Supplementary information

Construction of amorphous Fe-doped CoOOH coated crystalline Co2Mo3O8 heterostructure for stable and efficient oxygen evolution

Liangliang Lyu [1, 2], Chen Li [1, 2], Yuexin Gu [1, 2], Kaibo Hu [2], Jiuyang Lin [1, 2], Xu Zhao [3], Yinhua Wan * [1, 2], Xuewei Li * [1, 2]

1. School of Rare Earths, University of Science and Technology of China, Hefei 230026, P. R. China;

2. Ganjiang Innovation Academy, Chinese Academy of Sciences, Ganzhou 341000, P. R. China;

3. Research Center for Eco-Environmental Sciences, Chinese Academy of Sciences, Beijing 100085, P. R. China

*Corresponding Author
E-mail: yhwan@gia.cas.cn; xwli@gia.cas.cn

Experimental section

Materials

Nickel foam (NF), deionized (DI) water (H_2O), Sodium molybdate dihydrate ($Na_2MoO_4 \cdot 2H_2O$), Cobalt(II) nitrate hexahydrate ($Co(NO_3)_2 \cdot 6H_2O$), Iron(III) nitrate nonahydrate ($Fe(NO_3)_3 \cdot 9H_2O$), hydrochloric acid (HCl), sodium chloride (NaCl), sodium hydroxide (NaOH), Ethanol (CH3CH2OH), Cetyl trimethyl ammonium bromide (CTAB), Ammonium fluoride (NH_4F), Tetramethylammonium hydroxide (TMAOH), potassium hydroxide (KOH) were analytical grade and used without further treatment. The seawater used for testing comes from the Bohai Sea in China.

Pretreatment of nickel foam

NF (2 cm × 3 cm) was ultrasonically cleaned sequentially in 1 M KOH, 1 M HCl, and deionized water for 15 minutes each to obtain pretreated nickel foam。

Synthesis of CoMo precursor

1.25 mmol $Co(NO_3)_2 \cdot 6H_2O$, 1.25 mmol $Na_2MoO_4 \cdot 2H_2O$ and 20 mg CTAB were dissolved in 30 mL deionized water and stirred for 30 min. Then the obtained solution and the pretreated NF were transferred into a 50 mL Teflon-lined autoclave. Hydrothermal reaction was conducted at 180℃ for 12 h. Finally, the product was retrieved at room temperature, ultrasonically cleaned with deionized water and ethanol for 15 minutes each, and subsequently dried at 60℃ Celsius for 2 h. The resulting sample was named CoMo precursor.

Synthesis of CMONF

The obtained CoMo precursor was calcined in a mixed gas of 5% H_2 and 95% Ar at 500℃ for 2 h, and the resulting sample was named CMONF

Synthesis of FeCMONF

The CMONF was immersed in a 60 mL aqueous solution with 3 mmol $Fe(NO_3)_3 \cdot 9H_2O$ and 10 mmol NH_4F at 80°C for 120 seconds, and the resulting sample was named FeCMONF.

Synthesis of Fe-CoOOH

1.5 mmol $Co(NO_3)_2 \cdot 6H_2O$, 0.5mmol $Fe(NO_3)_3 \cdot 9H_2O$ and 5 mmol NH_4HCO_3 were dissolved in 60 mL deionized water and stirred for 30 min. Subsequently, a piece of NF (2 cm × 5 cm) was immersed in the solution at room temperature for 12 h. The deposited samples were electrochemically oxidized by cyclic voltammetry (CV) between 0.3 and 0.9 V (*vs*. Hg/HgO) in 1 M KOH at 5 mV s^{-1} for 10

cycles, followed by rinsing and drying to obtain Fe-CoOOH.

Synthesis of Pt/C/NF and IrO_2/NF

Pt/C/NF was prepared by dispersing 5 mg of Pt/C (20 wt% Pt) into 950 μL of water/ethanol (v/v = 10:9) mixture and 50 μL of 5 w.t.% Nafion through sonication for 60 min. Then 200 μL Pt/C ink was dispersed onto Ni foam of 1 cm^2 in geometric area. The IrO_2/NF was obtained using a method that is similar with the preparation of Pt/C/NF.

Characterization

X-ray diffraction (XRD, D8 Advance, Bruker AXS., German), Raman (inVia, Renishaw., England), and X-ray photoelectron spectroscopy (XPS, AXIS SUPRA+, Shimadzu Corporation., England) were used to detect the crystalline phase, microstructure, and the states of elements on the surface of samples. The scanning electron microscopy (SEM, CLARA GMH, Tescan., Czech Republic), transmission electron microscopy (TEM, JEM-F200, JEOL Ltd., Japan) and energy dispersive X-ray spectroscopy (EDS) were used to characterize the surface morphology of samples.

Electrochemical test

Electrochemical characterizations were performed in 1.0 M KOH solution at 25 ℃. Linear sweep voltammetry (LSV) was carried out with a CHI 760F workstation (CH instruments 760F) and performed at 2.0 mV s^{-1}. The sample, carbon rod electrode and Hg/HgO electrode are used as work electrode, counter electrode and reference electrode respectively. The measured potentials were aligned to the reversible hydrogen electrode (RHE) using the following equation (1):

$$E(\text{vs. RHE}) = E(\text{vs. Hg/HgO}) + 0.098 + 0.0591*\text{pH V}$$

The iR compensation potential (E_{com}) was obtained by the equation (2):

$$E_{com} = E_{mea} - iR_s$$

where E_{mea} and R_s were the measured potential and solution resistance, respectively.

The Tafel slope was calculated with the Tafel formula (3):

$$\eta = a + b\log|j|$$

where j, a and b were the current density, intercept and Tafel slope, respectively. Electrochemical impedance spectroscopy (EIS) was performed from 100 k to 0.1 Hz at 1.495 V vs. RHE.

The electrochemical double-layer capacitances (C_{dl}) in the non-faradaic potential region were calculated using CV curves with scanning rates of 20, 40, 60, 80, and 100 mV s^{-1}, respectively. The electrochemically active surface area (ECSA) can be calculated by equation (4):

$ECSA = C_{dl}/C_s$

The specific capacitance value of C_s is selected as 0.040 mF cm^{-2} for a smooth surface electrode.

Energy consumption for H_2 production

The energy consumption (EC) to produce 1 Nm^3 H_2 was calculated as:

$$Q = N \times F \times 2e^-$$

$$EC = (1000 \times Q \times E) / (N \times 22.4 \times 3.6 \times 10^6)\ kWh$$

$$Efficiency = HHV / EC$$

where Q is the charge, N is the moles of H_2, F is Faraday constant, $2e^-$ is the electron charge, and E is the applied voltage. The molar volume of gas was taken as 22.4 L mol^{-1}. The H_2 higher heating value (HHV) was taken as 3.575 kWh Nm^{-3}.

First-principles calculations

First-principles density functional theory (DFT) calculations were carried out to investigate the structural optimization, adsorption energies, and oxygen evolution reaction (OER) activity of the composite systems Fe-CoOOH/$Co_2Mo_3O_8$, CoOOH/$Co_2Mo_3O_8$, and the individual Fe-CoOOH catalyst. All calculations were performed using CP2K-2024[1], with simulation setup and post-processing handled by the Atomic Simulation Environment (ASE)[2]. The exchange-correlation energy was treated using the Becke–Lee–Yang–Parr (B3LYP) hybrid functional[3, 4], which provides an accurate description of electronic interactions in transition-metal oxide systems. The Gaussian and Plane-Wave (GAPW) method[5] was employed to combine the efficiency of Gaussian basis functions with the systematic convergence of plane-wave expansions. The Goedecker–Teter–Hutter (GTH) pseudopotentials[6] were used for core-electron treatment, and the def2-TZVP basis set[7] was used for all elements. A plane-wave cutoff energy of 1200 eV was adopted to ensure convergence of total energies. Γ-point (gamma-point) sampling was used for Brillouin zone integration due to the large size of the surface slabs. To account for long-range van der Waals interactions critical for surface chemistry and adsorption, Grimme's DFT-D3 dispersion correction[8] was employed throughout all calculations. Initial crystal structures of Fe-CoOOH and $Co_2Mo_3O_8$ were constructed based on experimental lattice data, and surface terminations were cleaved along the low-index (001) and (100) facets. For the heterostructures Fe-CoOOH/$Co_2Mo_3O_8$ and CoOOH/$Co_2Mo_3O_8$, interface models were created by aligning the lattice-matched surfaces, followed by full relaxation of all atomic positions using the Broyden–Fletcher–Goldfarb–Shanno (BFGS) algorithm until the force

on each atom was below 0.02 eV/Å and the energy change was less than 10^{-5} Ha. Bader charge analysis[9] was performed to evaluate charge redistribution upon adsorption and at the heterointerfaces. The density of states (DOS) and projected density of states (PDOS) were computed to analyze the d-band centers of Co, Fe, and Mo atoms and correlate them with the binding strength of intermediates. All geometry preparation, energy decomposition, and charge analyses were performed using ASE and custom Python scripts. Visualization was carried out using VESTA[10].

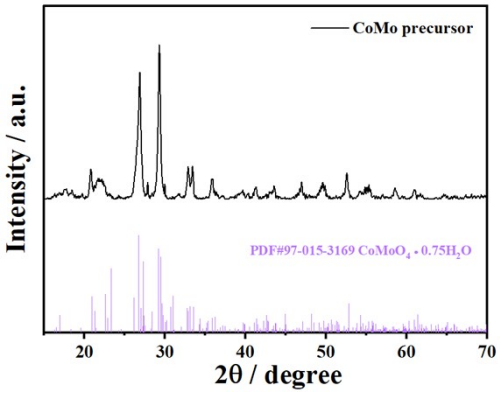

Fig S1. XRD pattern of CoMo precursor

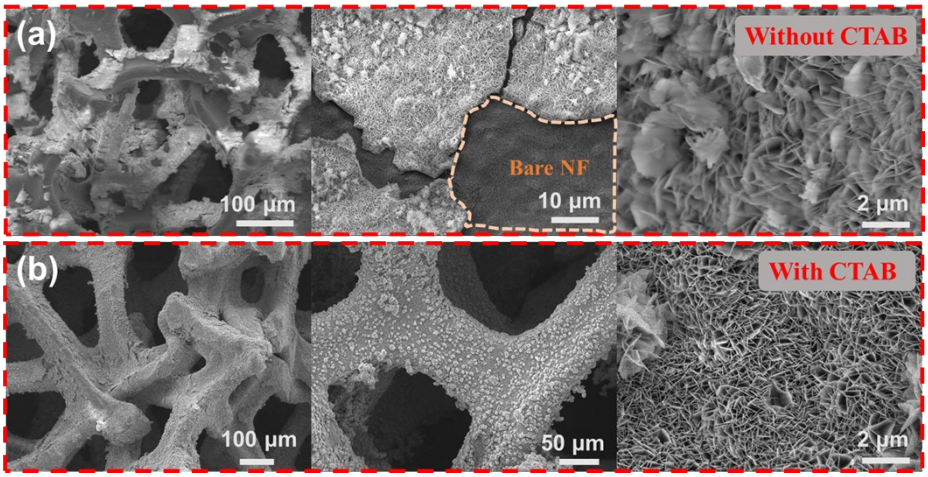

Fig S2. SEM images of CoMo precursor prepared with and without CTAB

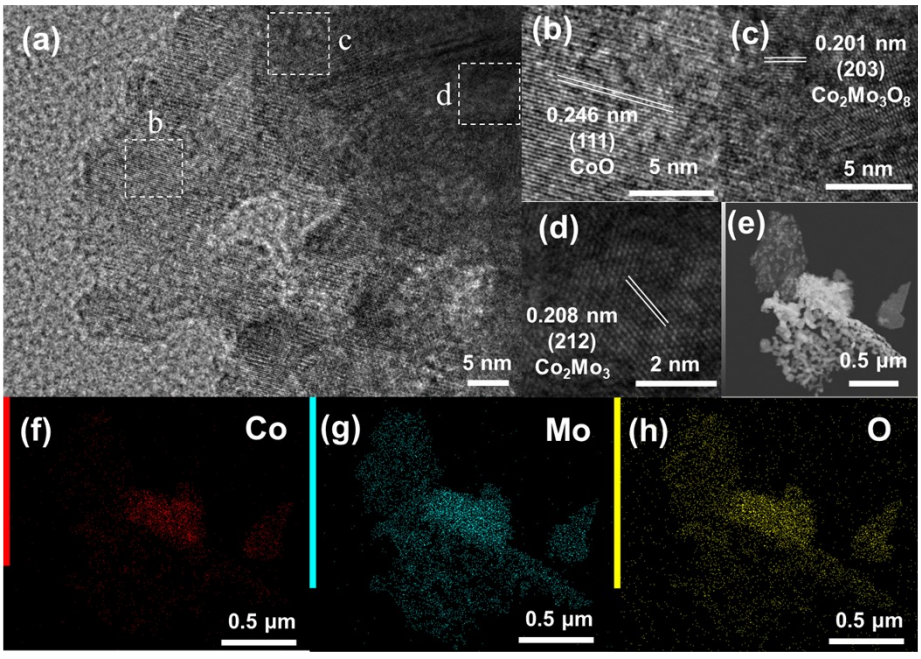

Fig S3. (a-d) HRTEM and (e-h) EDS mapping images of CMONF.

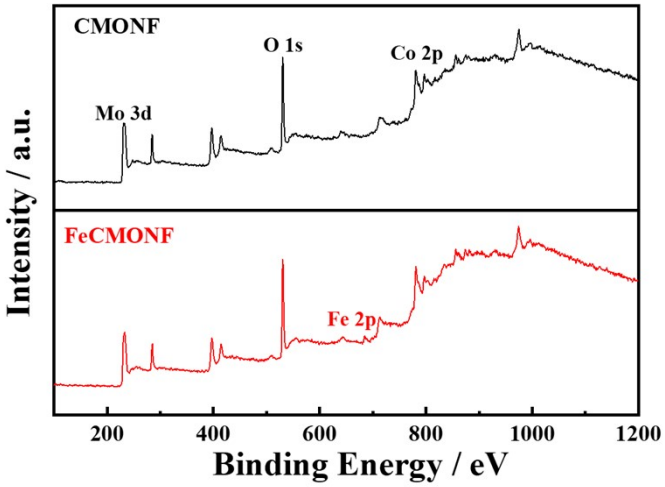

Fig S4. XPS survey spectra of CMONF, and FeCMONF.

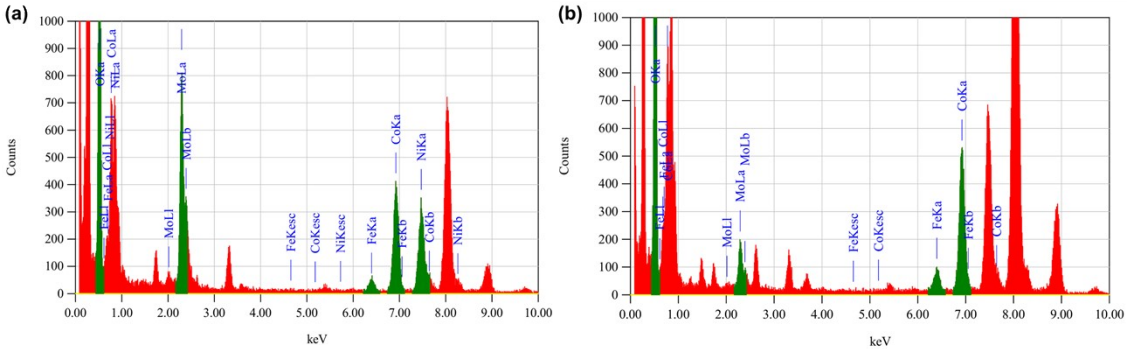

Fig S5. TEM-EDS images of (a) FeCMONF and (b) R-FeCMONF.

Table S1. EDS results of FeCMONF and R-FeCMONF.

Catalysts	Co wt%	Mo wt%	Fe wt%	O wt%
FeCMONF	27.03	39.38	1.33	32.26
R-FeCMONF	37.43	10.13	2.47	49.97

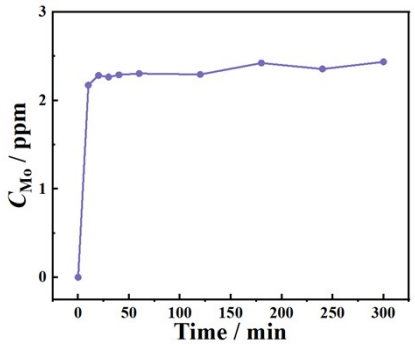

Fig S6. Time-dependent variation of Mo concentration in the electrolyte (sample: FeCMONF, j = 250 mA cm^{-2})

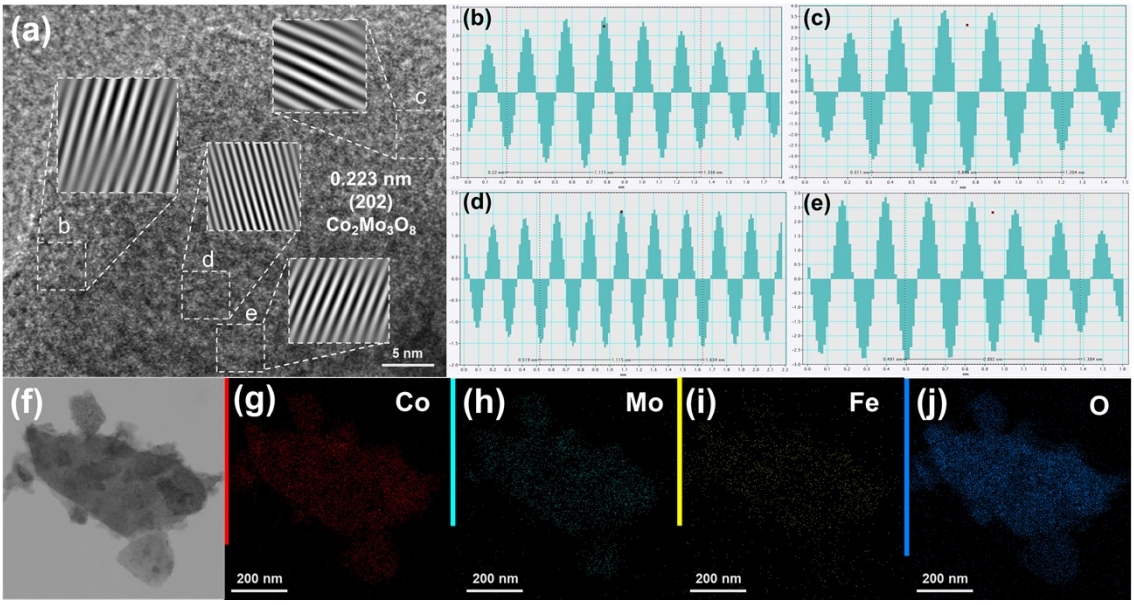

Fig S7. (a) HRTEM image, (b-e) integrated pixel intensities, and (f-j) EDS mapping images of R-FeCMONF.

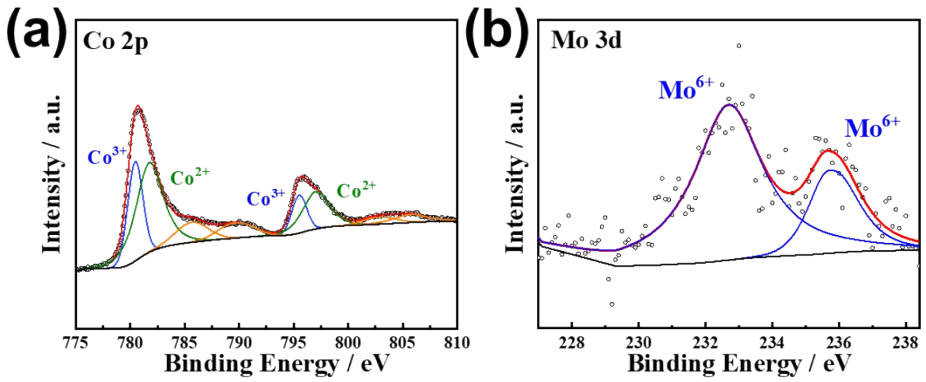

Fig S8. XPS spectra of (a) Co 2p, and (b) Mo 3d of R-FeCMONF

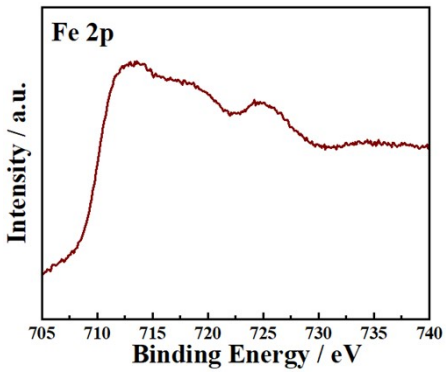

Fig S9. XPS spectra of Fe 2p of R-FeCMONF

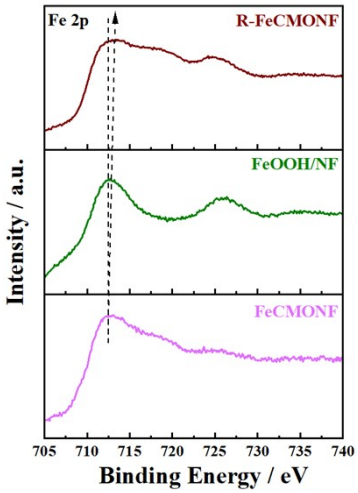

Fig S10. XPS spectra of Fe 2p of R-FeCMONF, FeOOH/NF, and FeCMONF.

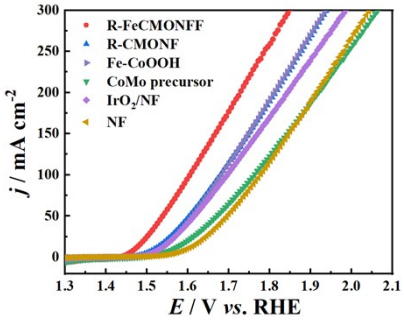

Fig S11. OER polarization curves of prepared samples without IR compensation.

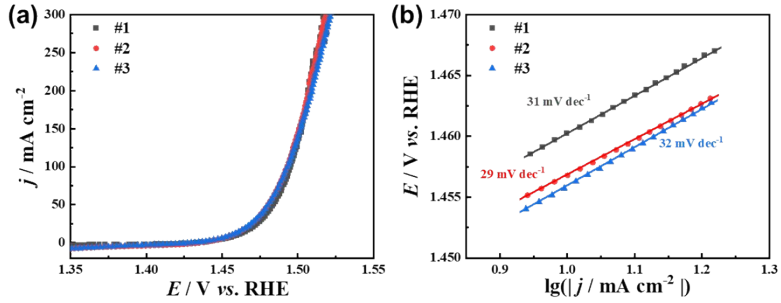

Fig S12. The repeatability test of (a) LSV curves and (b) Tafel slopes for R-FeCMONF.

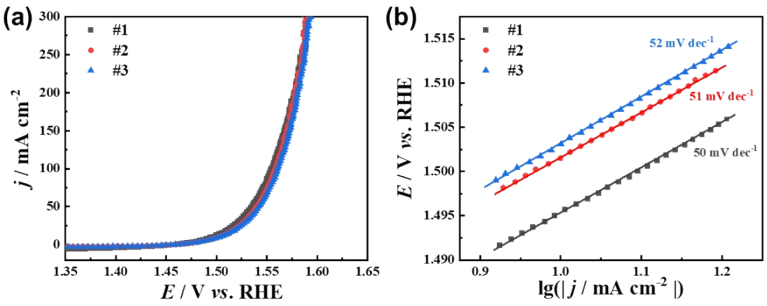

Fig S13. The repeatability test of (a) LSV curves and (b) Tafel slopes for R-CMONF.

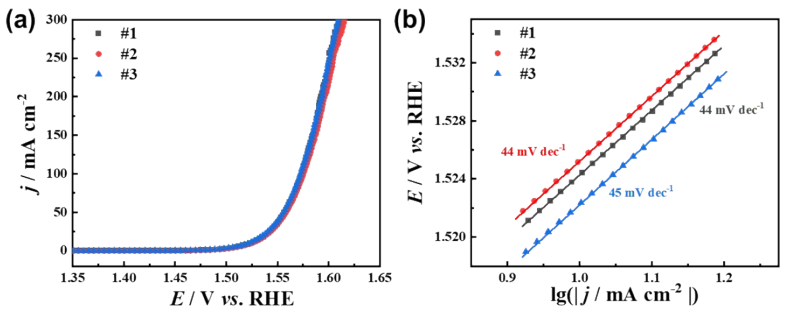

Fig S14. The repeatability test of (a) LSV curves and (b) Tafel slopes for Fe-CoOOH.

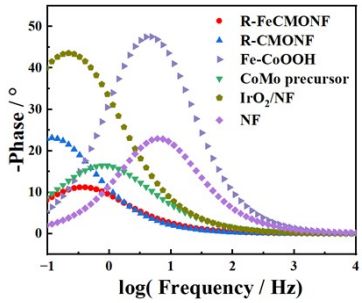

Fig S15. Bode plots of prepared samples.

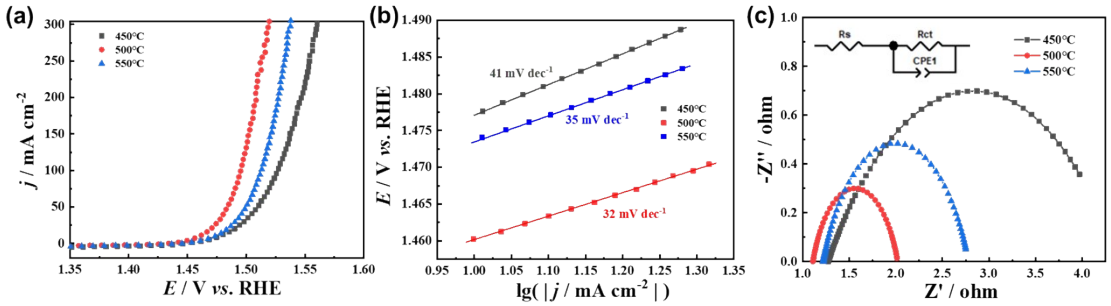

Fig S16. (a) Polarization curves, (b) Tafel slopes, and (c) Nyquist plots of R-FeCMONF. calcined in different temperature.

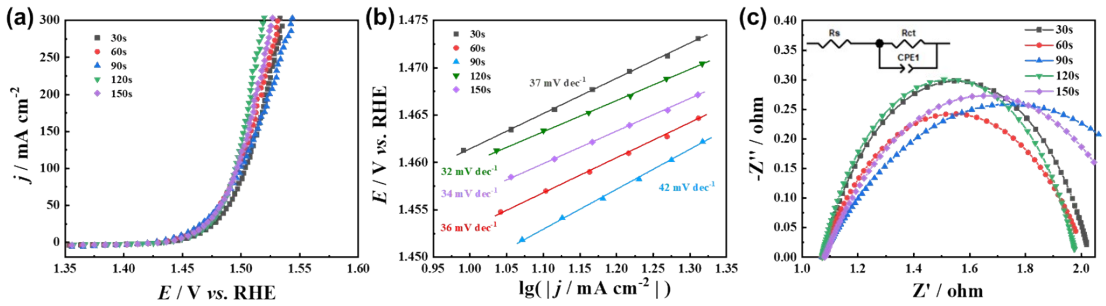

Fig S17. (a) Polarization curves, (b) Tafel slopes, and (c) Nyquist plots of R-FeCMONF. with different interfacial time.

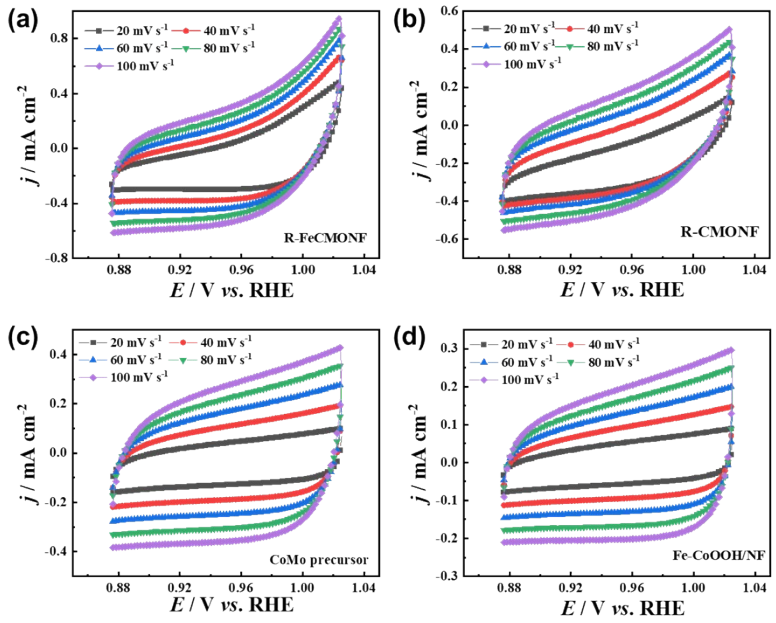

Fig S18. (a-d) CV curves at different scan rates.

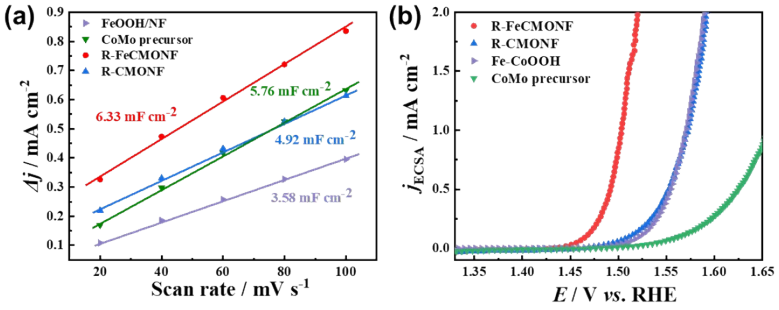

Fig S19. (a) C_{dl} curves; (b) OER polarization curves after ECSA normalization.

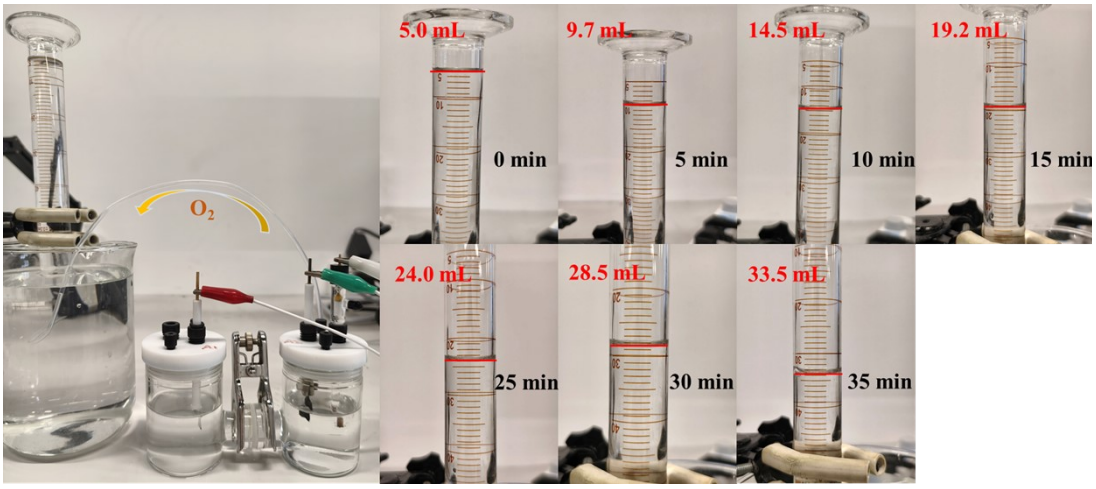

Fig S20. The change in O_2 production over time in 1 M KOH at 250 mA cm^{-2}.

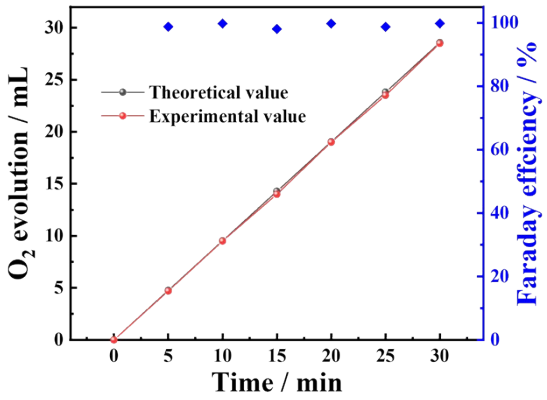

Fig S21. The oxygen production yield compared to the theoretical value, and the Faradaic efficiency of OER in 1 M KOH at 250 mA cm^{-2}.

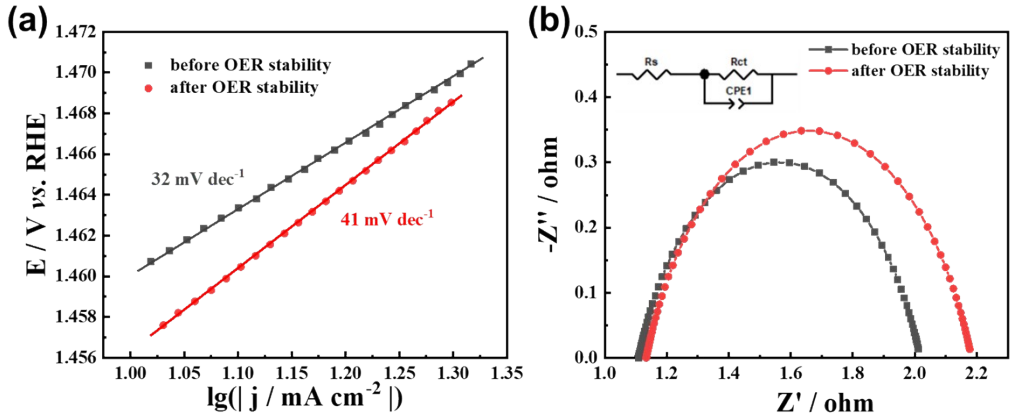

Fig S22. (a) Tafel slopes, and (b) Nyquist plots of R-FeCMONF. before and after OER in 1M KOH at 250 mA cm^{-2} for 280 h.

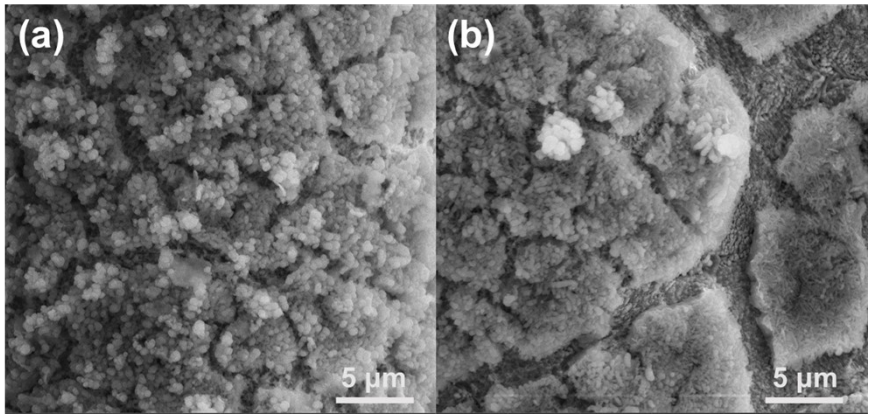

Fig S23. SEM images of R-FeCMONF (a) before and (b) after chronopotentiometry in 1 M KOH at 250 mA cm^{-2} for 280 h.

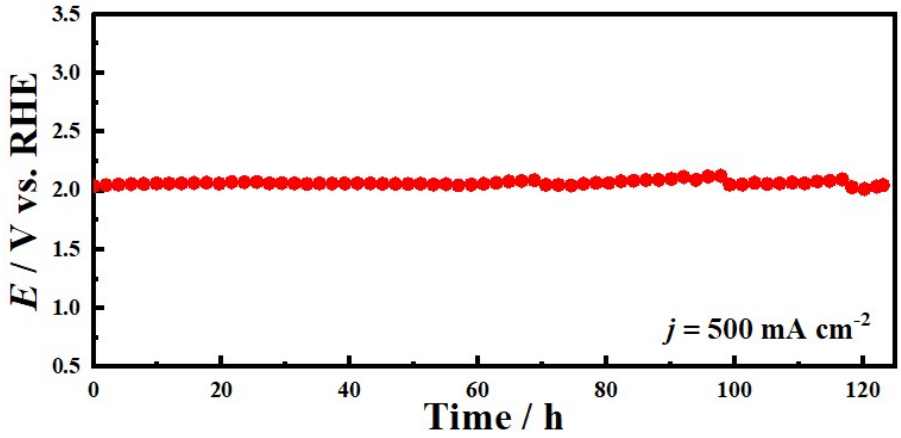

Fig S24. Chronopotentiometry of R-FeCMONF in 1 M KOH at 500 mA cm^{-2} without iR compensation.

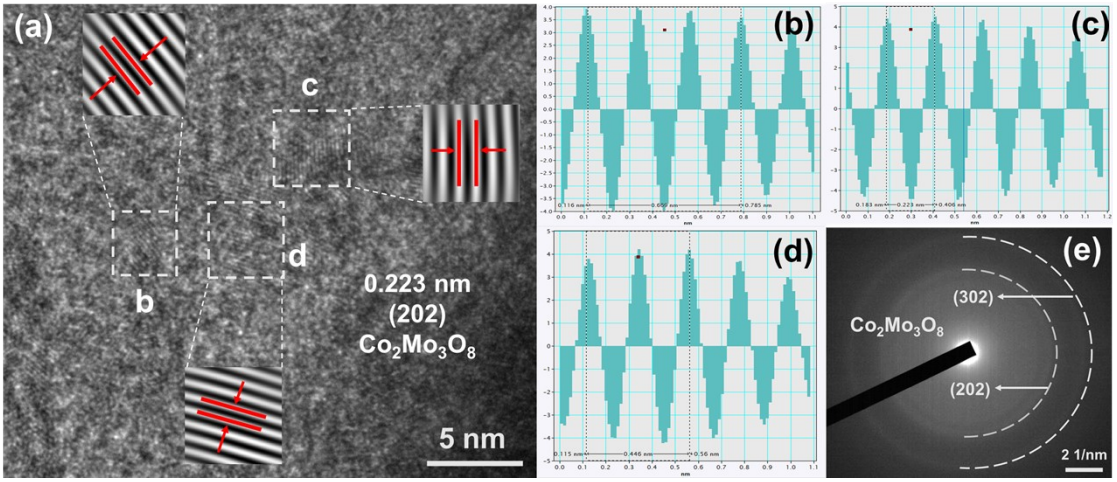

Fig S25. (a) HRTEM images of R-FeCMONF after chronopotentiometry in 1 M KOH, (b-d) integrated pixel intensities, and (e) SAED pattern of R-FeCMONF after chronopotentiometry in 1 M KOH.

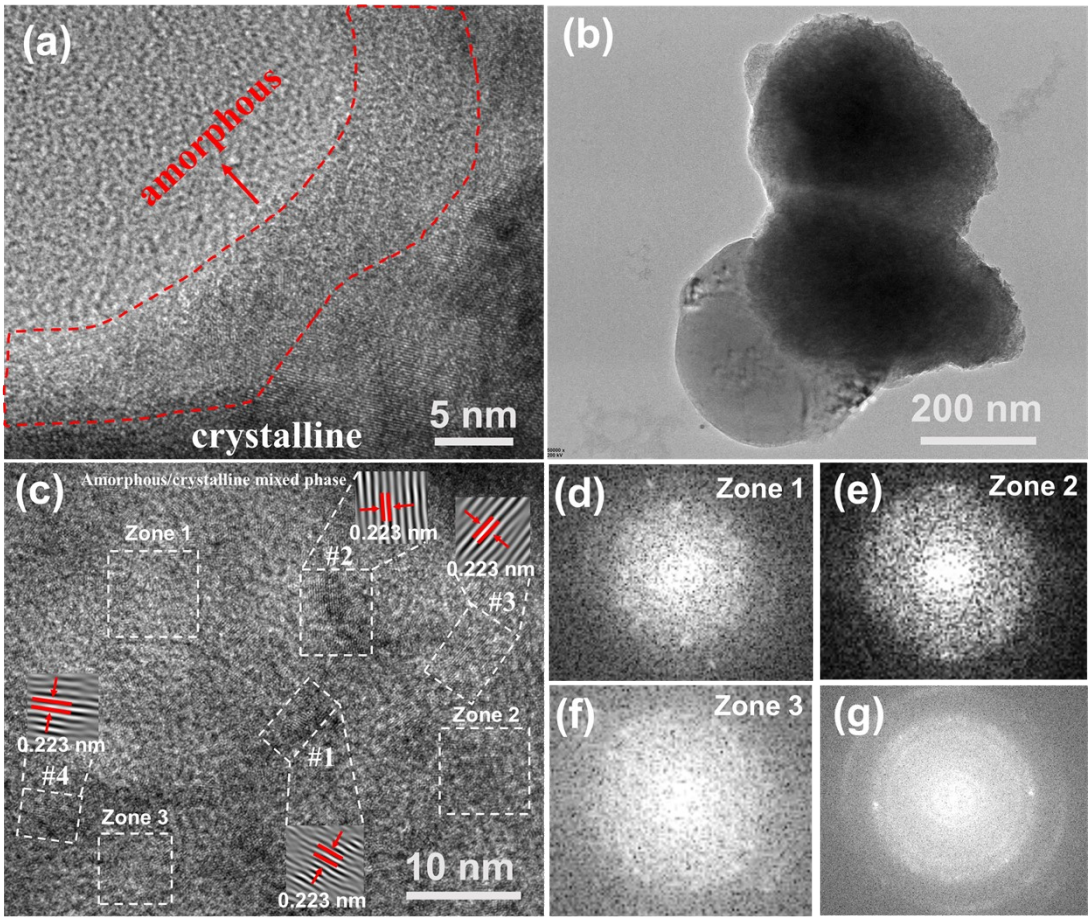

Fig S26. (a) HRTEM images of FeCMONF, (b-c) TEM images of R-FeCMONF after chronopotentiometry at 250 mA cm^{-2} in 1 M KOH for 280 h, (d) FFT of Zone 1, (e) FFT of Zone 2, (f) FFT of Zone 3, and (g) FFT of (c).

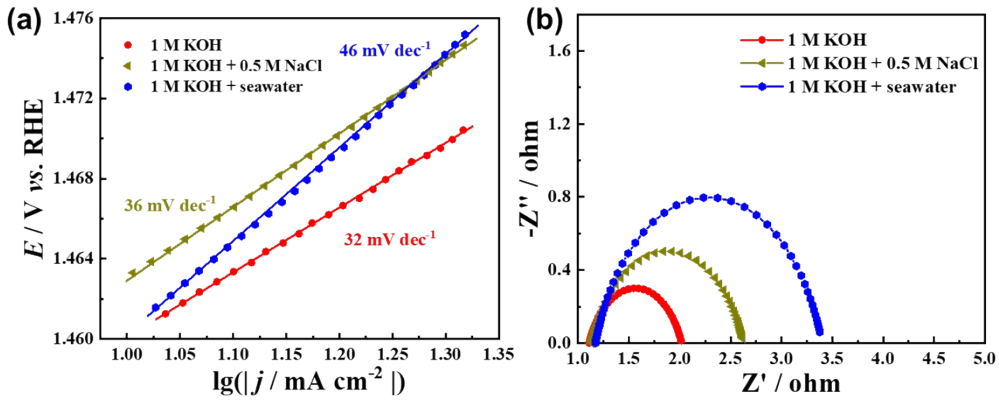

Fig S27. (a) Tafel slopes, and (b) Nyquist plots of R-FeCMONF. in different electrolytes.

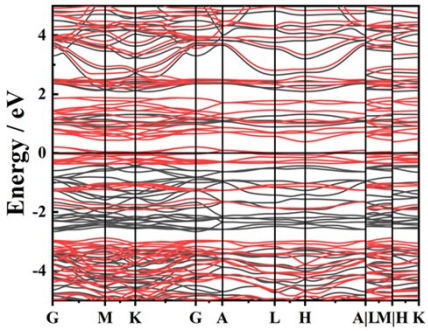

Fig S28. Band structure of $Co_2Mo_3O_8$.

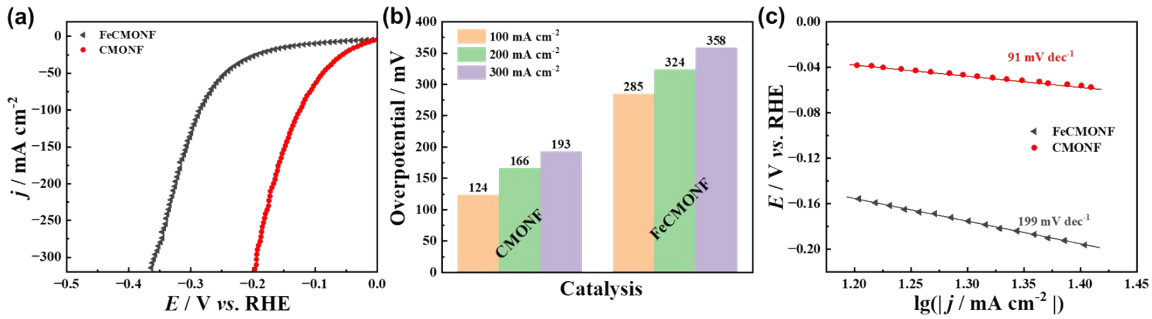

Fig S29. (a) Polarization curves of samples for HER, (b) comparison of HER overpotential, and (c) Tafel slopes of the samples in 1 M KOH.

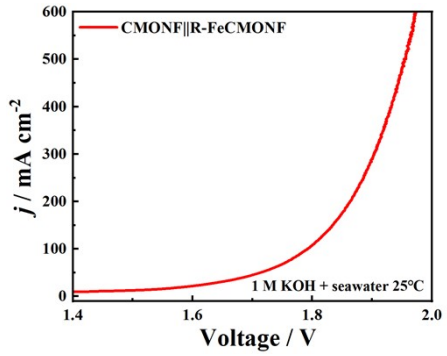

Fig S30. The polarization curves in alkaline natural seawater

Table S2. The overpotential and Tafel slope from the repetitive LSV curves.

Sample	Overpotential (mV) @10 mA cm^{-2}	Overpotential (mV) @100 mA cm^{-2}	Overpotential (mV) @300 mA cm^{-2}	Tafel slope (mV dec^{-1})
R-FeCMONF	223.7 ± 3.2	259.0 ± 2.0	275.0 ± 1.7	30.7 ± 1.5
R-CMONF	270.0 ± 3.6	328.0 ± 3.6	361.0 ± 3.5	51.0 ± 1.0
Fe-CoOOH	293.7 ± 1.5	343.7 ± 1.5	381.7 ± 3.1	44.3 ± 0.6

Table S3. EIS fitting data for samples.

Sample	R_s	CPE-T	CPE-P	R_{ct}
R-FeCMONF	1.109	0.78693	0.74407	0.9089
R-FeCMONF - after stability	1.139	0.61141	0.77198	1.023
R-CMONF	1.158	0.84881	0.76136	2.852
Fe-CoOOH	1.126	0.015684	0.88361	10.8
CoMo precursor	1.240	0.26093	0.75935	1.846
IrO_2/NF	1.369	0.1845	0.8347	12.75
NF	1.214	0.14144	0.82246	20.59

Table S4. The OER performance of recently reported transition-metal electrodes in 1 M KOH

Catalysts	***j*** **(mA cm^{-2})**	***η*** **(mV)**	**Tafel slope (mV dec^{-1})**	**Ref.**
R-FeCMONF	**10/100/300**	**220/264/286**	**32**	**This work**
NiFe-LDH/Ni_4Mo	100	264	42	11
SnS_2/MoS_2/TiO_2	10	271	58	12
HEMS	10	222	55.5	13
$FeCo_{0.41}Mn_{0.42}$ PBA	10/50	260/304	48	14
Vo-$CoMoVO_x$	10	248	74.2	15
R-NiFeOOH@SO_4	100	251	56	16
R-$CoMoO_4$/Co_3O_4@CC	10	250	60.5	17
Mg/Fe-N-C	10/20/30	224/240/250	51.74	18
FeOOH/NiSH/NF	50	256	73.8	19

FeP_4/CoP/C	10	258	41	20
$Zn_{0.5}Fe$/NF	100	250	60.1	21
$FeCo_{0.68}OOH$-$Pd_{0.026}$	10/100	265.1/313.9	37.5	22
$NiMoO_4$(Fe)	100	281.1	46.1	23
Ni-FeOOH	10/50	239/264	33	24
FeOOH/Ni_3S_2/NF	100	268	73	25
Ni-$FeWO_4$@WO_3/NF-1	10	235.01	60.47	26

Table S5. The overall water splitting performance

System	***j*** **(mA cm^{-2})**	***E*** **(V)**	**electrolyte**	**Ref.**
R-FeCMONF||CMONF	**20/100**	**1.49/1.65**	**1 M KOH**	**This work**
ZIF-67-D||ZIF-67-D	20	1.83	1 M KOH	27
P-V-NiFe LDH NSA||P-V-NiFe LDH NSA	20	1.53	1 M KOH	28
R-$CoMoO_4$/Co_3O_4@CC||Pt/C	10	1.51	1 M KOH	17
3D r-FeOOH/α-$Ni(OH)_2$/NF||3D r-FeOOH/α-$Ni(OH)_2$/NF	100	1.73	1 M KOH	29
CoMoOS-100/NF||Pt/C/NF	10	1.58	1 M KOH	30
pt-NFS||pt-NFS	10	1.51	1 M KOH	31
P-CMO/NF-400||P-CMO/NF-400	10	1.54	1 M KOH	32
P − $CoMo_2S_4$/Co_4S_3–Co_2P||P − $CoMo_2S_4$/Co_4S_3–Co_2P	10/100	1.55/1.74	1 M KOH	33

References

1 J. Hutter, M. Iannuzzi, F. Schiffmann and J. VandeVondele, *Wiley Interdisciplinary Reviews. Computational Molecular Science*, 2014, **4**, 25.

2 A. Hjorth Larsen, J. Jørgen Mortensen, J. Blomqvist, I. E. Castelli, R. Christensen, M. Dułak, J. Friis, M. N. Groves, B. Hammer, C. Hargus, E. D. Hermes, P. C. Jennings, P. Bjerre Jensen, J. Kermode, J. R. Kitchin, E. Leonhard Kolsbjerg, J. Kubal, K. Kaasbjerg, S. Lysgaard, J. Bergmann Maronsson, T. Maxson, T. Olsen, L. Pastewka, A. Peterson, C. Rostgaard, J. Schiøtz, O. Schütt, M. Strange, K. S. Thygesen, T. Vegge, L. Vilhelmsen, M. Walter, Z. Zeng and K. W. Jacobsen, *Journal of Physics: Condensed Matter*, 2017, **29**, 273002.

3 A. D. Becke, *Phys Rev A Gen Phys*, 1988, **38**, 3098-3100.

4 C. Lee, W. Yang and R. G. Parr, *Physical Review B*, 1988, **37**, 785-789.

5 B. G. Lippert, J. H. Parrinello and Michele, *Molecular Physics*, 2010, **92**, 477-488.

6 S.Goedecker, M.Teter and J.Hutter, *Physical Review B*, 1996, **54**, 1703-1710.

7 F. Weigend and R. Ahlrichs, *Physical Chemistry Chemical Physics*, 2005, **7**, 3297.

8 S. Grimme, J. Antony, S. Ehrlich and H. Krieg, *The Journal of Chemical Physics*, 2010, **132**, 154104.

9 G. Henkelman, A. Arnaldsson and H. Jónsson, *Computational Materials Science*, 2006, **36**, 354-360.

10 K. Momma and F. Izumi, *Journal of Applied Crystallography*, 2011, **44**, 1272-1276.

11 F. Wu, F. Tian, M. Li, S. Geng, L. Qiu, L. He, L. Li, Z. Chen, Y. Yu, W. Yang and Y. Hou, *Angewandte Chemie International Edition*, 2024, **64**, e202413250.

12 K. K. Mandari, Y.-A. Lee, S. Pandey, Y. Im, M. Altaf and M. Kang, *International Journal of Hydrogen Energy*, 2025, **105**, 116-125.

13 F. Qian, L. Peng, D. Cao, W. Jiang, C. Hu, J. Huang, X. Zhang, J. Luo, S. Chen, X. Wu, L. Song and Q. Chen, *Joule*, 2024, **8**, 2342-2356.

14 C. Wu, J. Wang, J. Li, H. Zhang, S. Sharma, L. Titheridge, C. Tiffin, Y. Fan, L. Zhao, W. Yang, Z. Li, J. Peng, J. Wang and A. T. Marshall, *ACS Applied Materials & Interfaces*, 2024, **16**, 58703-58710.

15 N. Luo, A. Cai, J. Pei, X. Zeng, X. Wang and N. Yao, *Advanced Functional Materials*, 2025, **35**, 2425503.

16 X. Luo, H. Zhao, X. Tan, S. Lin, K. Yu, X. Mu, Z. Tao, P. Ji and S. Mu, *Nature Communications*, 2024, **15**, 8293.

17 J. Zhu, J. Chen, X. Li, K. Luo, Z. Xiong, Z. Zhou, W. Zhu, Z. Luo, J. Huang and Y. Li, *Journal of Energy Chemistry*, 2024, **92**, 383-393.

18. J. Zhang, Y. Zhao, W. Zhao, J. Wang, Y. Hu, C. Huang, X. Zou, Y. Liu, D. Zhang, X. Lu, H. Fan and Y. Hou, *Angewandte Chemie International Edition*, 2023, **62**, e202314303.

19 B.-R. Guo, M.-X. Chen, S.-W. Li, R.-H. Gao, B.-H. Sang, X.-Q. Ren, Z. Liu, X. Cao, J. Liu, Y.-N. Ding, P. Xu and Y. Xu, *Rare Metals*, 2024, **43**, 6394-6404.

20 P. Zhao, C. Peng, Y. Luo, L. Cheng, Z. Li and Z. Jiao, *Chemical Engineering Journal*, 2024, **483**, 149121.

21 N. Yu, J. Y. Lv, Z.-C. Guo, X.-J. Tian, Y.-S. Zhang, W.-J. Li, Y.-L. Zhou, Y.-M. Chai and B. Dong, *Chemical Engineering Journal*, 2024, **487**, 150253.

22 S. Yang, L. Lu, P. Zhan, Z. Si, L. Chen, Y. Zhuang and P. Qin, *Applied Catalysis B: Environment and Energy*, 2024, **355**, 124213.

23 H. Hao, J. Wang, Z. Wang, S. Shen, L. Xu, Z. Lv and B. Wei, *Applied Catalysis B: Environment and Energy*, 2025, **363**, 124814.

24 Y. Yan, K. Huang, J. Lin, T. Yang, P. Wang, L. Qiao, W. Cai and X. Zheng, *Applied Catalysis B:*

Environmental, 2023, **330**, 122595.
25 M. Chen, Y. Zhang, J. Chen, R. Wang, B. Zhang, B. Song and P. Xu, *Small*, 2024, **20**, 2309371.
26 S. Zhao, Y. Wang, Y. Hao, L. Yin, C. H. Kuo, H. Y. Chen, L. Li and S. Peng, *Advanced Materials*, 2023, **36**, 2308925.
27 T. Kuang, L. Deng, M. Liu, Y. Ding, W. Guo, Z. Cai, W. Liu and Z. X. Huang, *Adv Mater*, 2025, **37**, e2415616.
28 Y. Tang, Q. Liu, L. Dong, H. B. Wu and X.-Y. Yu, *Applied Catalysis B: Environmental*, 2020, **266**, 118627.
29 X. Cheng, J. Yuan, J. Cao, C. Lei, B. Yang, Z. Li, X. Zhang, C. Yuan, L. Lei and Y. Hou, *J Colloid Interface Sci*, 2020, **579**, 340-346.
30 H. Xu, H. Shang, C. Wang, L. Jin, C. Chen, C. Wang and Y. Du, *Applied Catalysis B: Environmental*, 2020, **265**, 118605.
31 W. Ahmad, Y. Hou, N. Ahmad, K. Wang, C. Zou, Z. Wan, S. Aftab, S. Zhou, Z. Pan, H. L. Gao, C. Liang, W. Yan, M. Ling and Z. Lu, *Small Methods*, 2024, **8**, e2301434.
32 J. Wang, J. Hu, C. Liang, L. Chang, Y. Du, X. Han, J. Sun and P. Xu, *Chemical Engineering Journal*, 2022, **446**, 137094.
33 K. Dong, D. T. Tran, X. Li, S. Prabhakaran, D. H. Kim, N. H. Kim and J. H. Lee, *Applied Catalysis B: Environment and Energy*, 2024, **344**, 123649.